Quasiparticle interference of surface states in the type-II Weyl semimetal WTe_2

Wenhan Zhang,[1] Quansheng Wu,[2] Lunyong Zhang,[3] Sang-Wook Cheong,[1,4] Alexey A. Soluyanov,[2,5] and Weida Wu[1,*]

[1]*Department of Physics and Astronomy, Rutgers University, Piscataway, New Jersey 08854, USA*

[2]*Theoretical Physics and Station Q Zurich, ETH Zurich, 8093 Zurich, Switzerland*

[3]*Laboratory for Pohang Emergent Materials, Max Plank POSTECH Center for Complex Phase Materials, Max Planck POSTECH/Korea Research Initiative, Pohang 790-784, Korea*

[4]*Rutgers Center for Emergent Materials, Rutgers University, Piscataway, New Jersey 08854, USA*

[5]*Department of Physics, St. Petersburg State University, St. Petersburg 199034, Russia*

(Received 5 May 2017; revised manuscript received 21 September 2017; published 13 October 2017)

A topological Weyl semimetal (TWS) is a metal where low-energy excitations behave like Weyl fermions of high-energy physics. Recently, it was shown that, due to the lower symmetry of condensed-matter systems, they can realize two distinct types of Weyl fermions. The type-I Weyl fermion in a metal is formed by a linear crossing of two bands at a point in the crystalline momentum space—Brillouin zone. The second type of TWSs host type-II Weyl points appearing at the touching points of electron and hole pockets, which is a result of tilted linear dispersion. The type-II TWS was predicted to exist in several compounds, including WTe_2. Several angle-resolved photoemission spectroscopy studies of WTe_2 were reported so far, having contradictory conclusions on the topological nature of observed Fermi arcs. In this paper, we report the results of spectroscopic imaging with a scanning tunneling microscope and first-principles calculations, establishing clear quasiparticle interference features of the surface states of WTe_2. Our paper provides strong evidence for surface-state scattering. Although the surface Fermi arcs clearly are observed, it is still difficult to prove the existence of predicted type-II Weyl points in the bulk.

DOI: 10.1103/PhysRevB.96.165125

I. INTRODUCTION

The Weyl fermion was predicted first in particle physics in the beginning of the quantum era [1]. Although an example of a Weyl fermion is still unknown in particle physics, in condensed matter, it was proposed theoretically to emerge in topologically nontrivial crystals [2–5]. The material hosting Weyl fermions is called a topological Weyl semimetal (TWS). Weyl fermions in these materials always emerge in pairs of opposite chirality, being either a source or a sink of Berry curvature. Consequently, they can only be annihilated in pairs, being otherwise stable to weak translation-preserving perturbations [6,7]. The first type of Weyl fermion was predicted and observed in the TaAs family of compounds [8–11]. It is formed by a linear crossing of the valence band and conduction band in the Brillouin zone (BZ). Its low-energy excited states behave like Weyl fermions of standard quantum field theory. The Fermi surface in type-I TWSs, formed by Weyl points, is always closed. Interestingly, in the surface spectrum, this results in the appearance of open Fermi arcs, connecting the projections of opposite chirality Weyl points to the surface. Besides, TWSs supposedly provide a condensed-matter realization of the chiral anomaly [12]. Shortly after the type-I Weyl fermions were realized, Ref. [13] proposed type-II TWSs in which the linear dispersion is tilted so that Weyl points appear at the touching points of electron and hole pockets. Unlike type-I Weyl points, these Weyl points always have an open Fermi surface (when the Hamiltonian is linear in momentum), resulting in the unusual chiral anomaly [14]. The type-II TWS was predicted in several transition-metal dichalcogenides: WTe_2 [13], $MoTe_2$ [15,16], and $Mo_xW_{1-x}Te_2$ [17].

TWSs present many interesting exotic properties, such as surface Fermi arcs [2,18] and unconventional magnetotransport phenomena due to the chiral anomaly [12,19–24]. Among the interesting properties of TWSs, the surface Fermi arc is a crucial property associated with the nontrivial topological nature of the bulk states. Therefore, visualizing such surface states and proving their topological origin, is one of the major efforts in the studies of TWS. Angle-resolved photoemission spectroscopy (ARPES) studies on both type-I (TaAs family) [9–11,25] and type-II TWSs (transition-metal dichalcogenides) [26–31] have provided evidence of surface states, but whether the appearance of these states is a result of type-II Weyl points in the bulk remained unanswered. Scanning tunneling microscopy (STM) is a powerful technique to characterize the surface states of TWSs via quasiparticle interference (QPI) from spectroscopy measurements [32,33]. It can measure both the occupied and the unoccupied states with excellent energy resolution, whereas ARPES accesses only occupied states normally. This motivated scanning tunneling spectroscopy (STS) on WTe_2 to visualize the QPI due to surface states.

STS measurments have been performed on several TWS materials, such as TaAs [34–36], NbP [37], and $MoTe_2$ [27]. However, despite several prior STM studies on WTe_2 [38,39], the clear evidence of surface states of WTe_2 above E_F is still absent. Due to coexistence of the electron and hole pockets with Weyl nodes near the Fermi energy, the bulk states also contribute significantly to the surface scattering, which complicates the identification of the surface states. Therefore, it is necessary to compare experimental QPI results with first-principles calculations to differentiate the QPI feature of surface states from that of bulk states.

In this paper, we used STM/STS to directly visualize QPI patterns of surface states from two distinct surfaces of

*Corresponding author: wdwu@physics.rutgers.edu

WTe_2 single crystals. For comparison, we also carried out density functional theory (DFT) calculations and obtained surface spectral weight maps as well as the corresponding spin-preserved joint density of states (JDOS) maps at various energies. The good agreement between DFT calculations and experiments confirms that the main QPI is from scattering between two surface Fermi arcs in the surface BZ. The solid evidence of surface states on WTe_2 will stimulate further investigation of the topological nature of surface states in TWS materials.

II. METHOD

High quality single crystals of WTe_2 were grown via the iodine vapor transport method. Tungsten powder (99.9%) and tellurium powders (99.9%) were well mixed and heated in an evacuated silica tube at 700 °C for 2 days; the synthesized product then was ground and heated at 750 °C for 2 days. The final pellet was ground into fine powders. The appropriate amounts of powders and iodine were sealed in an evacuated silica tube and put in a two-zone furnace with a temperature gradient of 50 °C between 850 and 800 °C for 1 week.

STM/STS measurements were carried out at 4.5 K in an Omicron LT STM with a base pressure of 1×10^{-11} mbars. An electrochemically etched tungsten tip was characterized on a single-crystal Au(111) surface. To differentiate two polar surfaces, one piece of a WTe_2 single crystal was cut into two halves, and one of them was flipped upside down. Then both samples were mounted on STM sample plates without changing their orientations. They were cleaved *in situ* in ultra-high vacuum at room temperature and then were transferred immediately into a cold STM head for measurements. Since WTe_2 single crystals are always in the single domain state, the cleaved surfaces of the flipped crystal are presumably opposite to the other one. The dI/dV grid mapping measurements were performed to probe the QPI of the surface states. The set point is $V_B = -0.1$ V, $I = 0.5$ nA. At each point, a full dI/dV spectrum was recorded by ramping V_B from -0.1 to 0.1 V with feedback off. The standard lock-in technique was utilized with a modulation frequency of $f = 455$ Hz and a modulation amplitude of $V_{\text{mod}} = 20$ mV. The Fourier transform (FT) of the dI/dV maps are mirror symmetrized about the q_y axis and then smoothed with a Gaussian function.

On the theoretical side, we performed electronic structure calculations using DFT as implemented in the Vienna *ab initio* simulation package [40] with projector augmented-wave basis sets [41] that included spin-orbit coupling. The Perdew-Burke-Ernzerhof functional [42] was used in the exchange-correlation potential. A $16 \times 10 \times 4$ Γ-centered k-point mesh was used for Brillouin-zone sampling, and the energy cutoff was set to 450 eV. Then Wannier-based projected tight-binding models [43–45] capturing all the s and d states of W and p states of Te were used to analyze the surface density of states. Surface spectra were calculated with the software package WANNIERTOOLS [46], which is based on the iterative Green's-function mechanism [47]. The spin-dependent JDOS were calculated as

$$J_s(\mathbf{q}) = \frac{1}{2} \sum_{\mathbf{k}} \sum_{i=0\text{–}3} \rho_i(\mathbf{k}) \rho_i(\mathbf{k}+\mathbf{q}), \tag{1}$$

where the total spectral density is $\rho_0(\mathbf{k}) = -\frac{1}{\pi}\text{Im}[\text{Tr}\, G_s(\mathbf{k},\epsilon_0)]$, $G_s(\mathbf{k},\epsilon_0)$ is the surface Green's function at momentum k and energy ϵ_0 relative to the Fermi energy, and the spin density is $\rho_i(\mathbf{k}) = -\frac{1}{\pi}\text{Im}\{\text{Tr}[\sigma_i G_s(\mathbf{k},\epsilon_0)]\}$, $i = 1$–3 with $\sigma_{1\text{–}3}$ being the Pauli matrices of the electron spin.

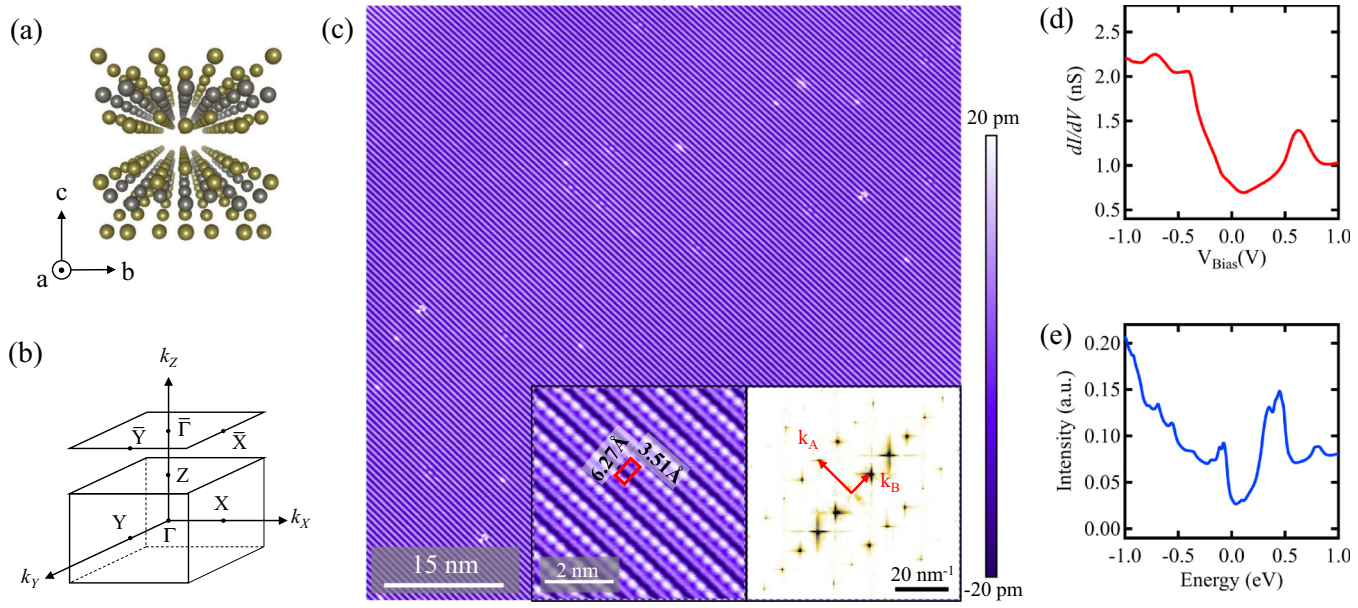

FIG. 1. (a) Crystal structure of WTe_2. (b) Schematics of bulk and surface BZs. (c) Large-scale topographic image of WTe_2. ($V_B = 1$ V, $I_T = 10$ pA) Left inset: Zoom-in topographic image ($V_B = 0.01$ V, $I_T = 2.4$ nA). Right inset: Fourier transform of the left inset image showing Bragg peaks corresponding to the atomic corrugation. (d) An average dI/dV spectrum taken on the WTe_2 surface ($V_B = -1$ V, $I_T = 1$ nA). (e) Calculated total density of states.

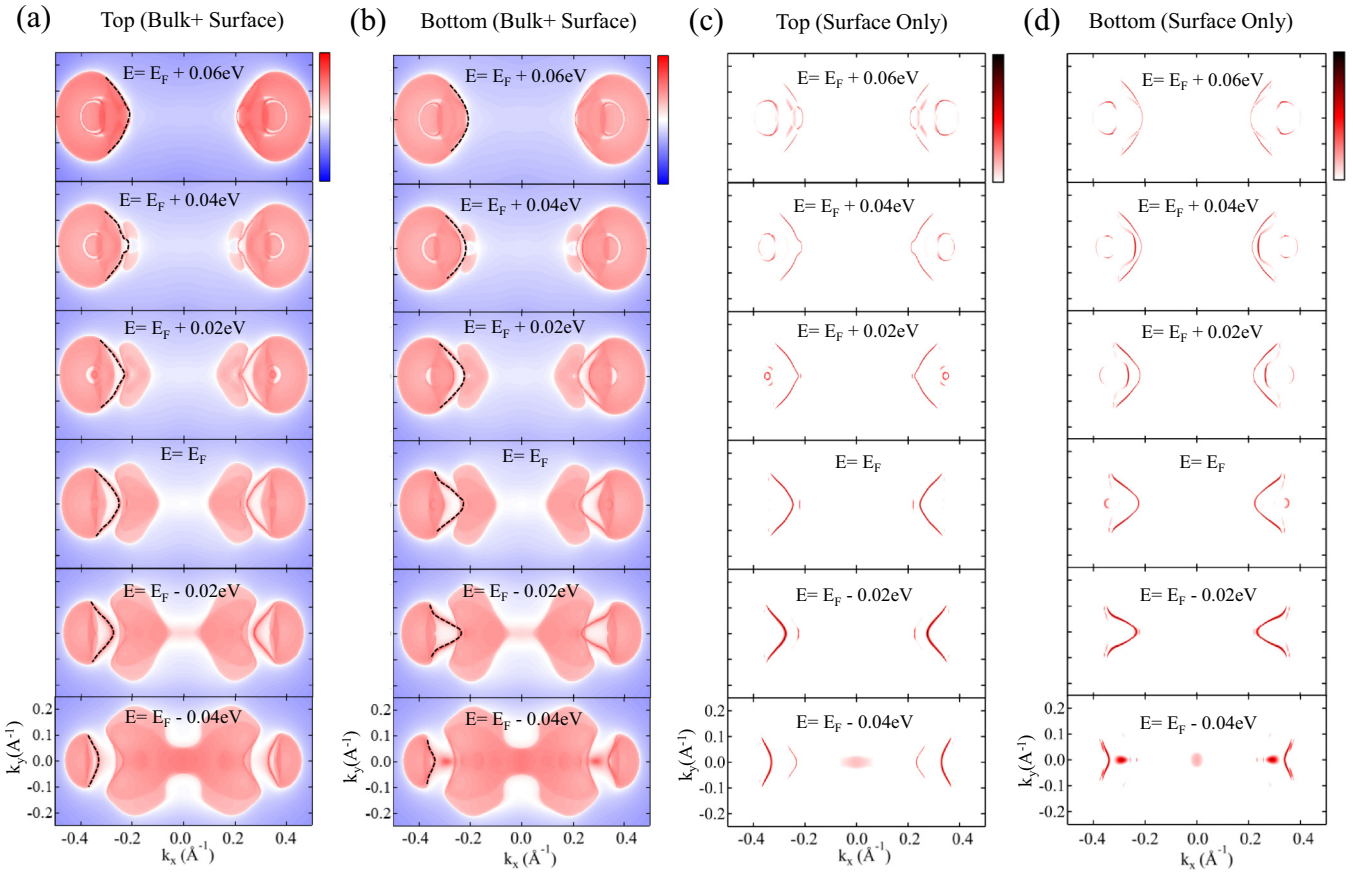

FIG. 2. Calculated spectral weight maps: the bulk states and surface states on (a) topmost and (b) bottommost (b) Te layers of WTe_2; the surface states only on (c) topmost and (d) bottommost Te layers of WTe_2. The energy is between $E_F - 40$ and $E_F + 60$ meV. The dashed lines indicate the surface Fermi arcs.

III. RESULTS

Figures 1(a) and 1(b) display the schematic bulk atomic structure and its Brillouin zone of WTe_2. Due to the lattice distortion, WTe_2 has an orthorhombic unit cell with the space-group $Pmn2_1$ [13,48]. Correspondingly, the surface Te atoms distort and form chains along the a axis as shown by large-scale topography in Fig. 1(c). In the zoom-in topographic image [the left inset of Fig. 1(c)], two inequivalent Te atomic chains are visible. The one with higher apparent height has better atomic resolution. The lattice constants estimated by the Bragg peaks in the right inset of Fig. 1(c) are $a = 3.51$ and $b = 6.27$ Å, which are consistent with the previous reports [38,48]. The orthorhombic lattice structure was observed repeatedly on multiple pieces of WTe_2 samples within our STM orthogonal uncertainty ($< 2^\circ$). The local density of states were measured by the dI/dV spectrum [Fig. 1(d)] showing a semimetallic behavior. The calculated total DOS of bulk WTe_2 [Fig. 1(e)] qualitatively agrees with the measurements.

Prior band-structure calculations of WTe_2 [48] reveal that both the valence band and the conduction band cross the Fermi level, forming electron and hole pockets. This has been confirmed by ARPES studies [49]. The calculations also predict that the Weyl points locate at around 50 meV above E_F [13]. Figures 2(a) and 2(b) plot the calculated spectral weight maps of bulk and surface states at various energies by projecting electronic states to the surface Te layers. The surface Fermi arcs are marked by the black dashed lines. The hole pockets locate closer to the Γ point than the Fermi arcs. As the energy increases, they shrink and disappear. The electron pockets, on the other hand, locate farther from the Γ point than the Fermi arcs. They grow larger at higher energies. In order to emphasize the surface states, projections from the bulk states have been removed. The spectral weight maps of the surface states are displayed in Figs. 2(c) and 2(d). Due to the broken inversion symmetry, the top and bottom surfaces of WTe_2 have inequivalent band structures. And this is confirmed by our calculated surface Fermi arcs on different surfaces. However, the dispersions of the surface Fermi arcs on these two surfaces are qualitatively the same. The surface Fermi arcs have nontrivial spin textures, which have been reported in Ref. [50]. They are most visible from $E_F - 40$ up to $E_F + 60$ meV. As the energy increases, the arclike surface states gradually move toward the Γ point (the BZ center). They completely disappear above $E_F + 60$ meV. It is in good agreement with constant energy contour results in ARPES experiments [28–30].

With the guidance of calculated spectral weight maps of the surface states, we performed spectroscopic grid mapping on two distinct surfaces of WTe_2 to investigate energy-dependent QPI patterns, which are the result of electrons being scattered elastically by defects. We locate a region on surface 1 with sufficient defect density as shown in Fig. 3(a). The fast

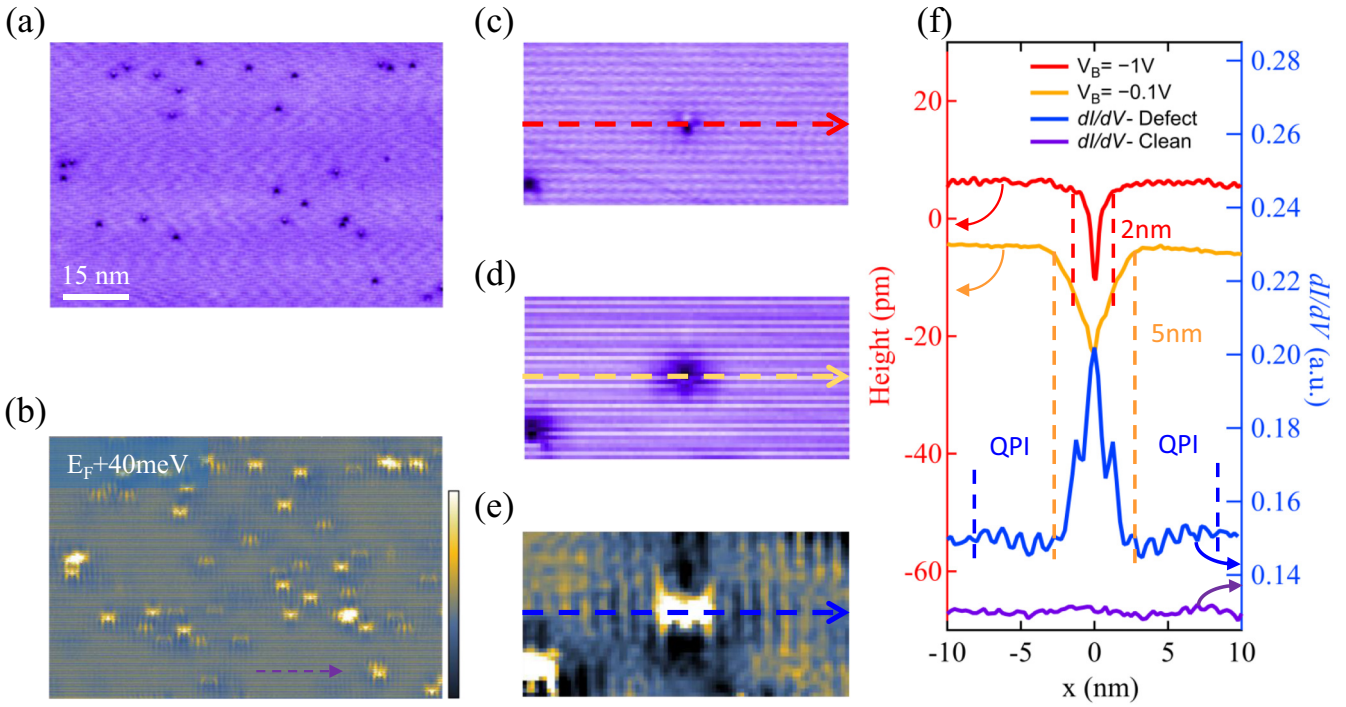

FIG. 3. (a) Topographic image where the dI/dV grid mapping was performed. ($V_B = -1$ V, $I_T = 100$ pA). (b) The dI/dV map at $E = E_F + 40$ meV in the same field of view as (a), showing quasiparticle scattering patterns around defects. (c) A zoom-in topographic image of an individual defect at $V_B = -1$ V. (d) A topographic image at $V_B = -0.1$ V in the same field of view as (c). (e) A dI/dV map at $E = E_F + 40$ meV in the same field of view as (c). (f) Line profiles of the topographic heights (red and orange) and dI/dV signals (blue). The positions where they were taken are marked by arrows in (c)–(e). The purple curve is the dI/dV line profile in the defect-free area as marked in (b).

scan axis is chosen to be parallel with the atomic chain (a axis). The major defects appear as surface suppression, indicating they may be subsurface vacancies or antisites. Clear spatial scattering around defects was observed in the dI/dV maps between -100 and $+100$ meV. Figure 3(b) displays a representative dI/dV map at $+40$ meV. Note that there are more scattering centers in the dI/dV map [Fig. 3(b)] than the surface defects observed in the topographic image of Fig. 3(a). They are probably defects underneath the surface Te layer. Two different patterns are observed commonly in the dI/dV maps at various energies: One is the dI/dV modulations localized on top of the defect cites [white spots at the center of Fig. 3(e)]; the other is the much weaker but extended standing waves around the defects. Figure 3(f) displays the line profiles taken on the topographic images [Figs. 3(c) and 3(d)] and the dI/dV map [Fig. 3(e)] across an isolated defect. The length scale of that localized dI/dV modulation is $l \sim 5$ nm, the same as the defect size, indicating that it is a result of impurity potential or defect states. In contrast, the oscillating pattern spreads about 17 nm away from the defects with a well-defined spatial periodicity of $\lambda \sim 1.1$ nm along the a direction, suggesting that it is the QPI pattern. Thus, based on the different length scales, the QPI pattern is separated unambiguously from the dI/dV modulations induced by the defect potential. The spectroscopic data of the other surface (not shown) present the same features.

FTs of the dI/dV maps in Figs. 4(a)–4(h) display the q (scattering wave vector) maps of QPI in the surface BZ in the energy range from 0 up to $+60$ meV. Several nontrivial features were observed: The red and green arrows point to a sharp pattern evolving towards the Γ point as the energies increase, and the purple arrows mark a nondispersive pattern that fades out gradually and disappears when $E > E_F + 40$ meV. The FT intensity around the Γ point is very high, but no sharp features are observed there. The sharp pattern locates at $q_x \sim 0.55$ Å^{-1}, equivalent to $\frac{2\pi}{\lambda}$, indicating its correspondence to the QPI shown in Fig. 3(f). Its dispersive character is illustrated manifestly in Fig. 4(r). As for the dI/dV modulation localized at the defect centers, the corresponding q value is about 0.13 Å^{-1}, which is much closer to the Γ point than the observed QPI. To understand the origins of these features in the q maps, the surface JDOS maps were calculated.

WTe_2 is a nonmagnetic type-II TWS. The time-reversal symmetry prevents scatterings between the states with opposite spins. This has been confirmed by STM studies of other nonmagnetic TWSs [27,34,37,51]. Therefore, the spin-preserving JDOS calculations are necessary to compare to the FTs of the dI/dV maps. Figures 4(i)–4(p) show the images of spin-preserved JDOS of surface states at the same energies with Figs. 4(a)–4(h). The X-shaped feature at the Γ point mainly originates from the intra-arc's scattering of the Fermi arcs, and the arclike features on the left and right sides correspond to the interarc scattering. As the energy increases, the interarc scattering features marked by the blue and orange arrows gradually move towards the Γ point. This trend is consistent with the evolving feature marked by the red and

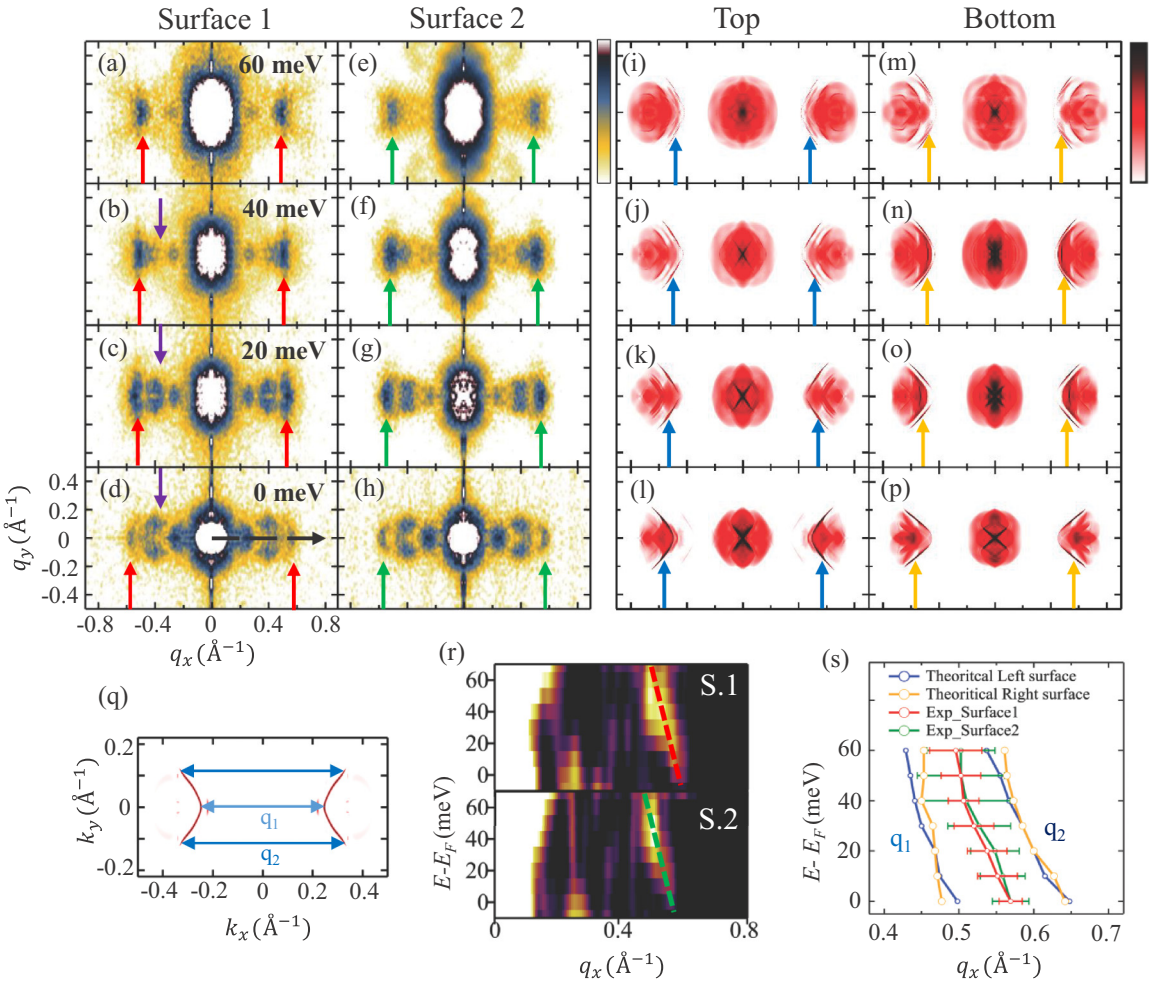

FIG. 4. (a)–(d) Fourier transforms of dI/dV maps taken on surface 1 from E_F to $E_F + 60$ meV. The red arrows point to interarc scattering features. The purple arrows point to the features generated by scattering between bulk states. (e)–(h) Fourier transforms of dI/dV maps taken on surface 2 in the same energy range. The green arrows point to interarc scattering features. (i)–(p) Calculated spin-preserving JDOS maps of surface states of both the topmost and the bottommost surfaces in the same energy range. The blue and orange arrows point to interarc scattering features. (q) Schematic of interarc scattering between two Fermi arcs in the BZ. q_1 and q_2 represent the head-to-head and tail-to-tail scattering vectors. (r) Experimental $E(q)$ dispersion along q_x axis on two surfaces. The red and green dashed lines mark the dispersion. (s) Dispersion of scattering vectors extracted from QPI patterns and comparison with calculated q_1 and q_2.

green arrows in the FTs of the dI/dV maps in Figs. 4(a)–4(h), suggesting that the red- and green-arrow patterns originate from the surface-state scattering.

To quantitatively compare the experimental QPI maps and calculated JDOS maps, the dispersions of the sharp pattern in Figs. 4(a)–4(h) are extracted and plotted together with the scattering vector obtained from DFT calculations as shown in Fig. 4(s). Here q_1 and q_2 represent the scattering vectors connecting the heads and tails, respectively, of the two Fermi arcs as illustrated by Fig. 4(q). With the presence of time-reversal symmetry, the states at the apex of the two Fermi arcs ($k_y = 0$) must have opposite spins, meaning the surface-state scattering q_1 is suppressed. Yet scattering vectors between q_1 and q_2 are allowed. The experimentally observed scattering vectors indeed fall in the range between q_1 and q_2 at various energies. The good agreement shows that the sharp feature captured in QPI patterns originates from scattering between surface states of Fermi arcs. In addition, the pattern marked by the purple arrows in Figs. 4(a)–4(h) does not associate with the surface-state scattering. It may result from the scattering between bulk states. Within the experimental uncertainty, the two surfaces present essentially identical QPI features. It is also consistent with our DFT calculation results that the two surfaces have qualitatively the same electronic structure.

IV. DISCUSSION AND CONCLUSION

It is still under debate whether the observed surface states are topological or trivial [28–30]. On one hand, small changes in lattice structure may change the topological nature of the material [29]. On the other hand, even in the topological phase, the trivial and topological surface states coexist and are in close proximity in k space, so it is very difficult to distinguish them experimentally. Furthermore, a recent work reported the Rashba spin splitting effect on the WTe_2 surface [38], suggesting that the trivial surface states may also be spin polarized. This makes it more difficult to identify the topological surface states unambiguously.

In conclusion, we combined STM/STS measurements and first-principles calculations to resolve the surface states on the (001) surface of WTe_2. The QPI patterns indicate the scattering of dispersive surface states. The calculated spin-dependent JDOS maps further confirm the existence of surface states on WTe_2. Our paper provides evidence of the surface states on type-II TWS WTe_2 and may inspire the subsequent research to figure out the topology of such surface states in semimetallic TWSs.

ACKNOWLEDGMENTS

We are grateful to J. Li, Z. Wang, and A. Bernevig for helpful discussions. The STM work at Rutgers was supported by NSF Grant No. DMR-1506618. The crystal growth work was supported partially by the NSF under Grant No. DMR-1629059. It was also supported by the Max Planck POSTECH/KOREA Research Initiative Program through the National Foundation of Korea (NRF) funded by the Ministry of Science, ICT, and Future Planning (Grant No. 2016K1A4A4A01922028). The calculation work was supported by the European Research Council through the ERC Advanced Grant SIMCOFE, the Swiss National Science Foundation, and through the National Competence Centers in Research MARVEL and QSIT. Q.W. and A.A.S. also acknowledge support from Microsoft Research.

W.Z. and Q.W. contributed equally to this work.

[1] H. Weyl, Z. Phys. **56**, 330 (1929).
[2] X. Wan, A. M. Turner, A. Vishwanath, and S. Y. Savrasov, Phys. Rev. B **83**, 205101 (2011).
[3] A. A. Burkov and L. Balents, Phys. Rev. Lett. **107**, 127205 (2011).
[4] D. Bulmash, C.-X. Liu, and X.-L. Qi, Phys. Rev. B **89**, 081106 (2014).
[5] J. Liu and D. Vanderbilt, Phys. Rev. B **90**, 155316 (2014).
[6] H. Nielsen and M. Ninomiya, Nucl. Phys. B **185**, 20 (1981).
[7] H. Nielsen and M. Ninomiya, Nucl. Phys. B **193**, 173 (1981).
[8] H. Weng, C. Fang, Z. Fang, B. A. Bernevig, and X. Dai, Phys. Rev. X **5**, 011029 (2015).
[9] S.-Y. Xu, I. Belopolski, N. Alidoust, M. Neupane, G. Bian, C. Zhang, R. Sankar, G. Chang, Z. Yuan, C.-C. Lee, S.-M. Huang, H. Zheng, J. Ma, D. S. Sanchez, B. Wang, A. Bansil, F. Chou, P. P. Shibayev, H. Lin, S. Jia, and M. Z. Hasan, Science **349**, 613 (2015).
[10] B. Q. Lv, H. M. Weng, B. B. Fu, X. P. Wang, H. Miao, J. Ma, P. Richard, X. C. Huang, L. X. Zhao, G. F. Chen, Z. Fang, X. Dai, T. Qian, and H. Ding, Phys. Rev. X **5**, 031013 (2015).
[11] B. Q. Lv, N. Xu, H. M. Weng, J. Z. Ma, P. Richard, X. C. Huang, L. X. Zhao, G. F. Chen, C. E. Matt, F. Bisti, V. N. Strocov, J. Mesot, Z. Fang, X. Dai, T. Qian, M. Shi, and H. Ding, Nat. Phys. **11**, 724 (2015).
[12] H. Nielsen and M. Ninomiya, Phys. Lett. B **130**, 389 (1983).
[13] A. A. Soluyanov, D. Gresch, Z. Wang, Q. Wu, M. Troyer, X. Dai, and B. A. Bernevig, Nature (London) **527**, 495 (2015).
[14] Y. Xu, F. Zhang, and C. Zhang, Phys. Rev. Lett. **115**, 265304 (2015).
[15] Y. Sun, S.-C. Wu, M. N. Ali, C. Felser, and B. Yan, Phys. Rev. B **92**, 161107(R) (2015).
[16] Y. Qi, P. G. Naumov, M. N. Ali, C. R. Rajamathi, W. Schnelle, O. Barkalov, M. Hanfland, S.-C. Wu, C. Shekhar, Y. Sun, V. Süß, M. Schmidt, U. Schwarz, E. Pippel, P. Werner, R. Hillebrand, T. Förster, E. Kampert, S. Parkin, R. J. Cava, C. Felser, B. Yan, and S. A. Medvedev, Nat. Commun. **7**, 11038 (2016).
[17] T.-R. Chang, S.-Y. Xu, G. Chang, C.-C. Lee, S.-M. Huang, B. Wang, G. Bian, H. Zheng, D. S. Sanchez, I. Belopolski, N. Alidoust, M. Neupane, A. Bansil, H.-T. Jeng, H. Lin, and M. Zahid Hasan, Nat. Commun. **7**, 10639 (2016).
[18] G. Xu, H. Weng, Z. Wang, X. Dai, and Z. Fang, Phys. Rev. Lett. **107**, 186806 (2011).
[19] A. A. Zyuzin and A. A. Burkov, Phys. Rev. B **86**, 115133 (2012).
[20] D. T. Son and B. Z. Spivak, Phys. Rev. B **88**, 104412 (2013).
[21] B. Z. Spivak and A. V. Andreev, Phys. Rev. B **93**, 085107 (2016).
[22] P. Hosur and X. Qi, C. R. Phys. **14**, 857 (2013).
[23] S. A. Parameswaran, T. Grover, D. A. Abanin, D. A. Pesin, and A. Vishwanath, Phys. Rev. X **4**, 031035 (2014).
[24] A. A. Burkov, J. Phys.: Condens. Matter **27**, 113201 (2015).
[25] L. X. Yang, Z. K. Liu, Y. Sun, H. Peng, H. F. Yang, T. Zhang, B. Zhou, Y. Zhang, Y. F. Guo, M. Rahn, D. Prabhakaran, Z. Hussain, S.-K. Mo, C. Felser, B. Yan, and Y. L. Chen, Nat. Phys. **11**, 728 (2015).
[26] L. Huang, T. M. McCormick, M. Ochi, Z. Zhao, M.-t. Suzuki, R. Arita, Y. Wu, D. Mou, H. Cao, J. Yan, N. Trivedi, and A. Kaminski, Nat. Mater. **15**, 1155 (2016).
[27] K. Deng, G. Wan, P. Deng, K. Zhang, S. Ding, E. Wang, M. Yan, H. Huang, H. Zhang, Z. Xu, J. Denlinger, A. Fedorov, H. Yang, W. Duan, H. Yao, Y. Wu, S. Fan, H. Zhang, X. Chen, and S. Zhou, Nat. Phys. **12**, 1105 (2016).
[28] Y. Wu, D. Mou, N. H. Jo, K. Sun, L. Huang, S. L. Bud'ko, P. C. Canfield, and A. Kaminski, Phys. Rev. B **94**, 121113 (2016).
[29] F. Y. Bruno, A. Tamai, Q. S. Wu, I. Cucchi, C. Barreteau, A. de la Torre, S. McKeown Walker, S. Riccò, Z. Wang, T. K. Kim, M. Hoesch, M. Shi, N. C. Plumb, E. Giannini, A. A. Soluyanov, and F. Baumberger, Phys. Rev. B **94**, 121112(R) (2016).
[30] C. Wang, Y. Zhang, J. Huang, S. Nie, G. Liu, A. Liang, Y. Zhang, B. Shen, J. Liu, C. Hu, Y. Ding, D. Liu, Y. Hu, S. He, L. Zhao, L. Yu, J. Hu, J. Wei, Z. Mao, Y. Shi, X. Jia, F. Zhang, S. Zhang, F. Yang, Z. Wang, Q. Peng, H. Weng, X. Dai, Z. Fang, Z. Xu, C. Chen, and X. J. Zhou, Phys. Rev. B **94**, 241119 (2016).
[31] J. Jiang, Z. Liu, Y. Sun, H. Yang, C. Rajamathi, Y. Qi, L. Yang, C. Chen, H. Peng, C.-C. Hwang, S. Sun, S.-K. Mo, I. Vobornik, J. Fujii, S. Parkin, C. Felser, B. Yan, and Y. Chen, Nat. Commun. **8**, 13973 (2017).
[32] S. Kourtis, J. Li, Z. Wang, A. Yazdani, and B. A. Bernevig, Phys. Rev. B **93**, 041109 (2016).
[33] G. Chang, S.-Y. Xu, H. Zheng, C.-C. Lee, S.-M. Huang, I. Belopolski, D. S. Sanchez, G. Bian, N. Alidoust, T.-R. Chang, C.-H. Hsu, H.-T. Jeng, A. Bansil, H. Lin, and M. Z. Hasan, Phys. Rev. Lett. **116**, 066601 (2016).

[34] H. Inoue, A. Gyenis, Z. Wang, J. Li, S. W. Oh, S. Jiang, N. Ni, B. A. Bernevig, and A. Yazdani, Science **351**, 1184 (2016).
[35] R. Batabyal, N. Morali, N. Avraham, Y. Sun, M. Schmidt, C. Felser, A. Stern, B. Yan, and H. Beidenkopf, Sci. Adv. **2**, e1600709 (2016).
[36] P. Sessi, Y. Sun, T. Bathon, F. Glott, Z. Li, H. Chen, L. Guo, X. Chen, M. Schmidt, C. Felser, B. Yan, and M. Bode, Phys. Rev. B **95**, 035114 (2017).
[37] H. Zheng, S. Xu, G. Bian, C. Guo, G. Chang, D. S. Sanchez, I. Belopolski, C.-C. Lee, S.-M. Huang, X. Zhang, R. Sankar, N. Alidoust, T.-R. Chang, F. Wu, T. Neupert, F.-C. Chou, H.-T. Jeng, N. Yao, A. Bansil, S. Jia, H. Lin, and M. Z. Hasan, ACS Nano **10**, 1378 (2016).
[38] Q. Li, J. Yan, B. Yang, Y. Zang, J. Zhang, K. He, M. Wu, Y. Zhao, D. Mandrus, J. Wang, Q. Xue, L. Chi, D. J. Singh, and M. Pan, Phys. Rev. B **94**, 115419 (2016).
[39] P. K. Das, D. Di Sante, I. Vobornik, J. Fujii, T. Okuda, E. Bruyer, A. Gyenis, B. E. Feldman, J. Tao, R. Ciancio, G. Rossi, M. N. Ali, S. Picozzi, A. Yadzani, G. Panaccione, and R. J. Cava, Nat. Commun. **7**, 10847 (2016).
[40] G. Kresse and J. Furthmüller, Comput. Mater. Sci. **6**, 15 (1996).
[41] P. E. Blöchl, Phys. Rev. B **50**, 17953 (1994).
[42] J. P. Perdew, K. Burke, and M. Ernzerhof, Phys. Rev. Lett. **77**, 3865 (1996).
[43] A. A. Mostofi, J. R. Yates, Y.-S. Lee, I. Souza, D. Vanderbilt, and N. Marzari, Comput. Phys. Commun. **178**, 685 (2008).
[44] N. Marzari and D. Vanderbilt, Phys. Rev. B **56**, 12847 (1997).
[45] I. Souza, N. Marzari, and D. Vanderbilt, Phys. Rev. B **65**, 035109 (2001).
[46] Q. Wu, S. Zhang, H.-F. Song, M. Troyer, and A. A. Soluyanov, arXiv:1703.07789.
[47] M. P. L. Sancho, J. M. L. Sancho, J. M. L. Sancho, and J. Rubio, J. Phys. F **15**, 851 (1985).
[48] M. N. Ali, J. Xiong, S. Flynn, J. Tao, Q. D. Gibson, L. M. Schoop, T. Liang, N. Haldolaarachchige, M. Hirschberger, N. P. Ong, and R. J. Cava, Nature (London) **514**, 205 (2014).
[49] I. Pletikosić, M. N. Ali, A. V. Fedorov, R. J. Cava, and T. Valla, Phys. Rev. Lett. **113**, 216601 (2014).
[50] B. Feng, Y.-H. Chan, Y. Feng, R.-Y. Liu, M.-Y. Chou, K. Kuroda, K. Yaji, A. Harasawa, P. Moras, A. Barinov, W. Malaeb, C. Bareille, T. Kondo, S. Shin, F. Komori, T.-C. Chiang, Y. Shi, and I. Matsuda, Phys. Rev. B **94**, 195134 (2016).
[51] H. Zheng, G. Bian, G. Chang, H. Lu, S.-Y. Xu, G. Wang, T.-R. Chang, S. Zhang, I. Belopolski, N. Alidoust, D. S. Sanchez, F. Song, H.-T. Jeng, N. Yao, A. Bansil, S. Jia, H. Lin, and M. Z. Hasan, Phys. Rev. Lett. **117**, 266804 (2016).